

Simulation and Experimental Validation of a Misaligned Rotor in Journal Bearings using Different Levels of Detail

A. Krinner, W. Tsunoda, C. Wagner, T. Berninger, T. Thümmel, D. Rixen

In this contribution, a given test rig of a rotor system with journal bearing is validated by using simulation models with different levels of detail. A special focus is placed on the misalignment between rotor and bearing axis. It is shown, how to consider misalignment in the numeric calculation of the bearing forces as well as in the modeling of the rotor system. With a model of the LAVAL rotor, the misalignment in the test rig is identified by measuring and simulating relative equilibrium positions of the rotor in the bearing at different rotational speeds. A measured rotor orbit due to unbalance is used to compare simulation results of different complex rotor models and discuss their accuracy and efficiency.

1 Introduction

The dynamic behavior of a rotor system with journal bearings, which operates at steady-state conditions like a constant rotational speed, strongly depends on its equilibrium position. At low rotational speeds, the equilibrium between gravity force, stiffness force and fluid force is found at a larger eccentricity than for higher rotational speeds, meaning that the rotor moves to the bearing center with increasing rotational speed. This fact is illustrated in Fig. 1(a) for the case of a vanishing stiffness force. Fig. 1(a) shows the equilibrium eccentricity e between shaft and bearing center in dependency of the rotational speed Ω , when vertical gravity force and the fluid force are the only acting forces in the bearing with clearance h_0 . The well-known GUEMBEL curve arises, see for instance [4, 11, 3]. In an idealized rotor bearing system, the rotor axis is assumed to be perfectly aligned with the bearing axis. In this case, the equilibrium position can be calculated by the equality of gravity, stiffness and fluid force. However, in reality, the rotor axis can be misaligned in the bearing housing, resulting in a different equilibrium position, since an additional misalignment force has to be considered in the static force equilibrium. As a consequence, misalignment affects the dynamic behavior of the rotor system and hence, it also needs to be considered in simulation models. To illustrate this fact, Fig. 1(b) sketches the equilibrium eccentricity in dependency of the rotational speed Ω for the case, in which the rotor stiffness and additionally, a misalignment a between rotor shaft and bearing axis are considered. It occurs a different curve of equilibrium positions compared to the curve of Fig. 1(a).

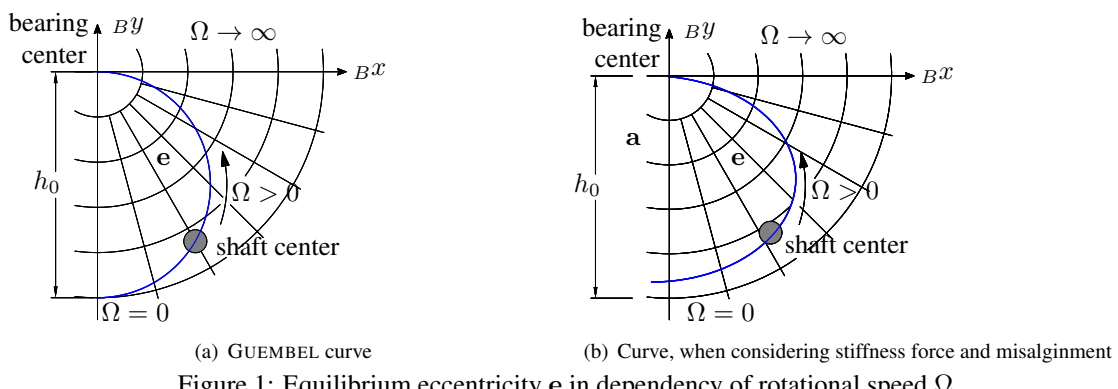


Figure 1: Equilibrium eccentricity e in dependency of rotational speed Ω .

Several contributions to a misaligned rotor system can be found in literature: The interaction between misalignment and wear is investigated by an analytical model in [9] and an experimental study on this interaction is given in [2]. In [12], a theoretical study on a misaligned shaft due to an external preload force is outlined. Angularly misaligned bearings are numerically investigated in [1]. In [7], a design of a test rig with a rotor supported by four journal

bearings suitable for the prediction of misalignment is proposed. In [10], simulation models and results for a flexible rotor system with angular and parallel misalignment are presented.

In this contribution, a rotor test rig with journal bearings is investigated with respect to parallel misalignment of rotor and bearing axis. First, a simple rotor model is applied in order to analyze the misalignment and in a next step, the dynamic behavior of the test rig due to unbalance can be investigated by further rotor models.

The paper is structured as follows: In Section 2, the hydrodynamic equations for the calculation of the fluid forces are outlined. Then, the rotor test rig with two journal bearings is described in Section 3. In Section 4, four different rotor models (LAVAL / elastic rotor with nonlinear / linearized fluid forces) are presented for the numeric simulation of the test rig. In Section 5, two experiments are validated by the different simulation models. While the first experiment serves to determine the misalignment, the second experiment is used for the evaluation of the different rotor models. At the end, a conclusion is given in Section 6.

2 Hydrodynamic Equations

In this section, the hydrodynamic equations for the calculation of the fluid forces in a hydrodynamic lubricated cylindrical joint are given. For a more detailed description, it is referred to [8].

The pressure is computed by a finite element discretization of the REYNOLDS equation, which is introduced first. A steady-state cavitation condition, also known as REYNOLDS condition, is imposed on the REYNOLDS equation in order to avoid negative pressures in the fluid film. It is further shown how to adapt the kinematics of the REYNOLDS equation to a cylindrical joint. Last, the calculation of the fluid forces is given.

REYNOLDS Equation

Fig. 2 shows a lubricated contact, which is characterized by a thin fluid film between the interface of two bodies. When the fluid inertia effects are neglected, the pressure distribution in the thin fluid film can be calculated by the REYNOLDS equation. It gives following partial differential equation for the pressure in the fluid film $h(y, z) = h_2 - h_1$ between the two bodies in the two-dimensional fluid domain $\Omega_f \subset \mathbb{R}^2$ with descriptive coordinates (y, z) (see for instance [6]):

$$\underbrace{-\frac{\partial}{\partial y} \left(\frac{h^3 \rho \partial p}{12\eta \partial y} \right) - \frac{\partial}{\partial z} \left(\frac{h^3 \rho \partial p}{12\eta \partial z} \right)}_{q_{\text{poiseuille}}} = \underbrace{-\frac{\partial}{\partial y} \left(\rho h \frac{v_1 + v_2}{2} \right)}_{-q_{\text{couette}}} - \underbrace{\rho \frac{\partial h}{\partial t}}_{-q_{\text{squeeze}}} - \underbrace{h \frac{\partial \rho}{\partial t}}_{-q_{\text{expansion}}} \quad (1)$$

where u_i and v_i are the absolute velocities of the interface of body i ($i \in \{1, 2\}$) in the local normal and tangential direction, respectively. For simplicity, the velocity w_i in z -direction is not considered here. It is also assumed that the fluid viscosity η and the fluid density ρ do neither depend on pressure nor on temperature. In Eq. (1), the POISEUILLE flow $q_{\text{poiseuille}}$ is driven by the pressure gradient, the COUETTE flow q_{couette} occurs due to the movement of surfaces in the tangential plane, the squeeze flow q_{squeeze} occurs due to squeezing motion and the local expansion flow $q_{\text{expansion}}$ occurs due to the change of density. The squeeze flow depends on the local normal velocities u_i , the tangential velocities v_i and derivatives of the heights h_i with respect to y , by the following equation (see [6]):

$$\frac{\partial h}{\partial t} = u_2 - v_2 \frac{\partial h_2}{\partial y} - u_1 + v_1 \frac{\partial h_1}{\partial y}. \quad (2)$$

A numerical discretization by the finite element method is applied to the REYNOLDS equation (1). For the discretized pressure \mathbf{P} , the following discretized equation can be obtained:

$$\mathbf{A}(\mathbf{q}) \mathbf{P} = \mathbf{b}(\mathbf{q}, \dot{\mathbf{q}}) - \mathbf{N} \mathbf{Q}_{\text{exp.}}, \quad (3)$$

where the kinematics of the two bodies are now described by the generalized coordinates \mathbf{q} and velocities $\dot{\mathbf{q}}$. The square matrix \mathbf{A} results from the numerical discretization of the POISEUILLE flow, the vector \mathbf{b} from the discretization of the terms $-q_{\text{couette}}$ and $-q_{\text{squeeze}}$ and the square matrix \mathbf{N} is the finite element mass matrix. The discretized expansion term $\mathbf{Q}_{\text{exp.}}$ is still unknown, but a cavitation condition in the next subsection gives an additional relation between pressure and expansion term. It is noted, that for the numerical discretization of the REYNOLDS equation, the standard GALERKIN method with quadrilateral finite elements (each with eight nodes) is applied and for all later simulation examples, a structured rectangular mesh with 16 elements in circumferential and 3 elements in z -direction respectively, is used.

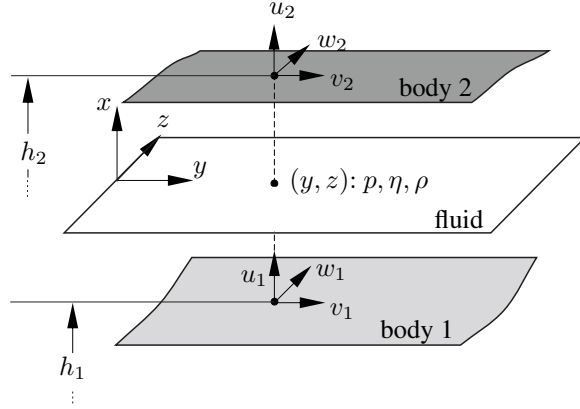


Figure 2: Notations in the fluid domain.

Cavitation Condition

Here, a stationary cavitation condition, also known as REYNOLDS condition, is imposed on the REYNOLDS equation (1) in order to eliminate the expansion term and further to avoid unphysical negative pressures in the fluid film. The REYNOLDS cavitation condition states that in the pressurized zone ($p > 0$) the change of density $\frac{\partial \rho}{\partial t}$ is zero (meaning $q_{\text{exp.}} = 0$), whereas in the cavitation zone ($p = 0$) the density starts to decrease, meaning $\frac{\partial \rho}{\partial t} < 0$, leading to a positive expansion term $q_{\text{exp.}} > 0$. This cavitation condition can be formulated mathematically by a Linear Complementarity Problem (LCP) by finding the pressure p such that:

$$0 \leq -q_{\text{exp.}} = \left(-\nabla \left(\frac{h^3 \rho}{12 \eta} \nabla p \right) + q_{\text{couette}} + q_{\text{squeezze}} \right) \perp p \geq 0 \quad \text{on } \Omega_f, \quad (4)$$

$$p = \hat{p} \quad \text{on } \Gamma_p, \quad (5)$$

$$\frac{h^3 \rho}{12 \eta} \nabla p \mathbf{n} = \hat{q} \quad \text{on } \Gamma_q, \quad (6)$$

where the symbol \perp denotes orthogonality for each point (y, z) on Ω_f (i.e. $q_{\text{exp.}}(y, z) \cdot p(y, z) = 0$). Dirichlet and Neumann boundary conditions are considered additionally in the REYNOLDS equation at the boundaries Γ_p and Γ_q respectively. With the discretized equation (3) follows:

$$\mathbf{0} \leq \mathbf{P} \perp -\mathbf{Q}_{\text{exp.}} \geq \mathbf{0} \quad \Leftrightarrow \quad \mathbf{0} \leq \mathbf{P} \perp \mathbf{N}^{-1} [\mathbf{A}(\mathbf{q}) \mathbf{P} - \mathbf{b}(\mathbf{q}, \dot{\mathbf{q}})] \geq \mathbf{0}, \quad (7)$$

where the symbol \perp stands now for component-wise orthogonality. This resulting LCP for the pressure \mathbf{P} can only be solved by different methods, e.g. a block pivot-based Murty algorithm of Goenka [5] or a projection formulation as proposed in [8].

Joint Kinematics

For a cylindrical revolute joint, the local kinematic entities can be derived according to Fig. 3. The procedure is explained for a two-dimensional problem, but it can without difficulty be extended to the three-dimensional case. In the cylindrical bearing, the local coordinates ($y = R\varphi, z$) are used for the description of the fluid domain. The joint kinematics is described in the frame (Bx, By), which is fixed to the bearing shell. For the REYNOLDS equation, local entities are needed, i.e. the velocities and heights have to be transformed into the local frame (Fx, Fy). For the eccentricity between the two center points C_1 and C_2 follows:

$$B\mathbf{e} = \begin{pmatrix} e_x \\ e_y \end{pmatrix} \rightarrow F\mathbf{e} = \begin{pmatrix} e_r \\ e_t \end{pmatrix} = \begin{pmatrix} e_x \cos(\varphi) + e_y \sin(\varphi) \\ -e_x \sin(\varphi) + e_y \cos(\varphi) \end{pmatrix}. \quad (8)$$

According to Fig. 3, following local heights h_1 and h_2 can be derived for the two points P_1 and P_2 , respectively:

$$h_1(y, z) = e_r(y, z) + \sqrt{R_1^2 - e_t^2(y, z)}, \quad (9)$$

$$h_2(y, z) = R_2. \quad (10)$$

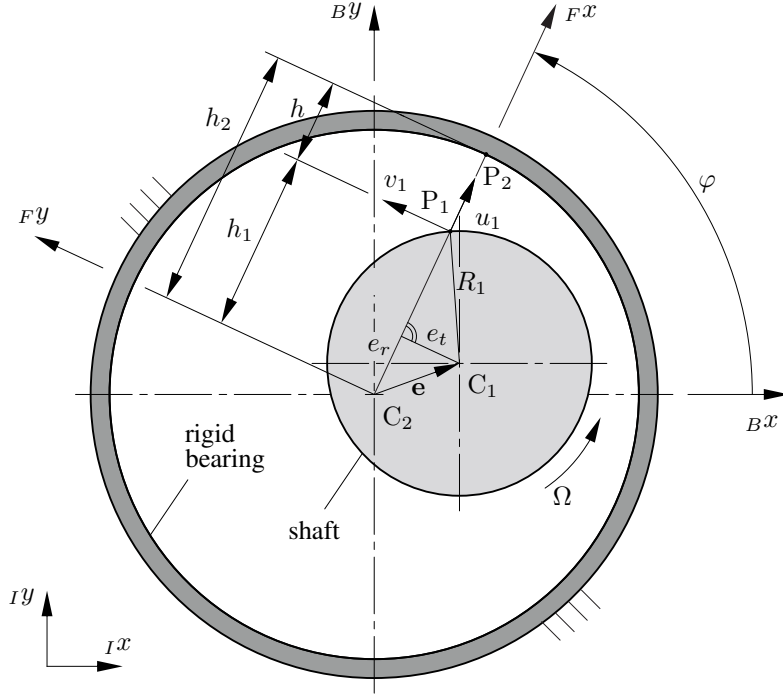


Figure 3: Kinematics in cylindrical joint.

For the local velocities, the translation velocities as well as the angular velocity vectors of the center point of shaft C_1 and bearing C_2 respectively are needed in the local (F_x, F_y) coordinate system. With them, following local velocities can be stated for a fixed bearing housing, according to Fig. 3:

$$u_1 = \Omega e_t + \dot{e}_x \cos(\varphi) + \dot{e}_y \sin(\varphi), \quad u_2 = 0 \quad (11)$$

$$v_1 = \Omega \sqrt{R_1^2 - e_t^2(y, z)} - \dot{e}_x \sin(\varphi) + \dot{e}_y \cos(\varphi), \quad v_2 = 0 \quad (12)$$

Having the kinematic entities as a function of the descriptive coordinates (y, z) , the derivatives of the local heights and velocities with respect to y can be derived for the REYNOLDS equation.

Force Calculation

When the pressure \mathbf{P} is known in the bearing by Eq. (7), the fluid forces on the two bodies can be computed. Here, it is shown only for pressure forces in normal direction, shear forces in tangential direction are not considered for simplicity. For the resulting force $\mathbf{F}_{f,i}$ on body i follows:

$$\mathbf{F}_{f,i} = \int_{\Omega_f} p \mathbf{n}_i d\Omega \approx \mathbf{W}(\mathbf{q})_i \mathbf{P}, \quad i \in \{1, 2\}, \quad (13)$$

where $\mathbf{W}(\mathbf{q})_i$ is the discrete direction matrix, which is state-dependent due to the normal directions \mathbf{n}_i .

3 Rotor Test Rig with two Journal Bearings

At the Institute of Applied Mechanics, a rotor test rig exists for the investigation of the interaction of the rotor dynamics with fluid forces coming from a journal bearing or a seal. In Fig. 4, the experimental setup is shown. It consists of an elastic rotor, which is supported by stiff roller bearings at the two ends. In the middle of the rotor, a rigid disk rotates in a pressurized journal bearing component system. This system consists of two identical journal bearings with external pressure support in the center of the two bearings, see Fig. 4. An oil distribution ring ensures an uniform oil flow through the bearings.

When pressurizing the journal bearing system at zero rotational speed, the rotor is lifted in an equilibrium position. In the following, this equilibrium position at zero rotational velocity is denoted by the misalignment parameter \mathbf{a} .

Further, it is assumed for simplicity that the lifting force due to the external pressure support remains constant in both its value and directions.

The main properties of the rotor test rig and the journal bearings are listed in Table 1. The bending stiffness of the dry rotor was identified by an operational modal analysis by determining the first bending eigenfrequency.

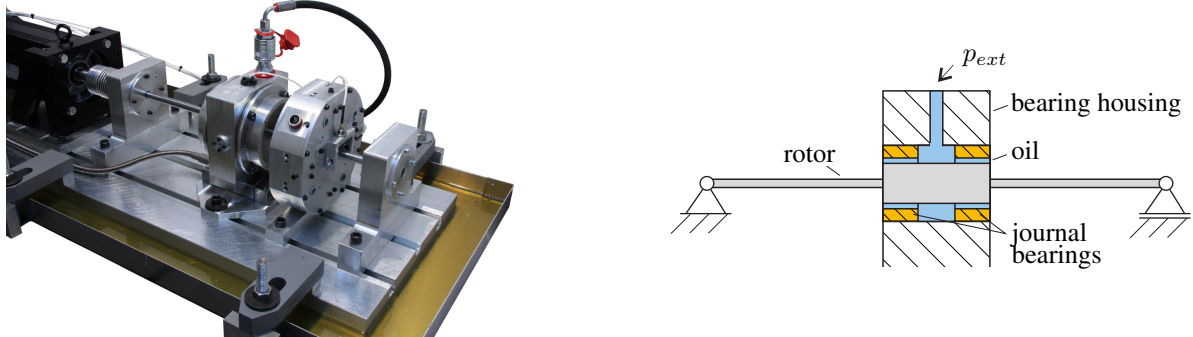


Figure 4: Rotor test rig with journal bearings.

Table 1: Properties of the test rig.

parameter	value	parameter	value	parameter	value
rotor mass m	5.0 kg	radius bearing R_2	50 mm	dyn. viscosity η	0.021 kg m/m ²
bending stiffness rotor c	295 kN/m	clearance bearing	170 μ m	fluid density ρ	880 kg/m ³
length rotor	0.60 m	length bearing	20 mm	external pressure p_{ext}	2.5 bar
1. eigenfrequency (dry)	38.6 Hz	diameter shaft	15 mm		

4 Rotor Modeling

In this section, different rotor models are presented for the validation of the experimental results. As the rotor axis in the test rig is not aligned concentrically to the bearing axis, misalignment is considered for all models. Further, it will be assumed that the gravity force is always compensated due to the external pressure support.

Four different complex rotor models are introduced. The first one is a LAVAL rotor with misalignment and fluid forces. This model will be used for the experimental validation of equilibrium positions of the rotor bearing system at different rotational speeds.

The further models are a LAVAL rotor with linearized fluid forces, a complete elastic rotor model with nonlinear and linearized fluid forces, respectively. These models will be used for comparisons with the first rotor model in order to discuss their model differences with respect to experimental measurements.

Model A1: LAVAL Rotor with Misalignment and Fluid Forces

The first model is a LAVAL rotor as depicted in Fig. 5. The rotor is characterized by the mass m and the stiffness c and its deflection \mathbf{r} is described in the inertia frame, which is located in the center of the undeformed shaft. The misalignment is considered by the vector \mathbf{a} as relative alignment between bearing axis and rotor axis at zero rotational speed. Then, following dynamic equations can be stated:

$$m \ddot{\mathbf{r}} + c \mathbf{r} = 2 \mathbf{F}_f(\mathbf{r}, \dot{\mathbf{r}}, \Omega, \mathbf{a}) + \mathbf{F}_p + \mathbf{F}_g + \mathbf{F}_{ext}, \quad (14)$$

where \mathbf{F}_f is the nonlinear fluid force of one journal bearing according to (13) depending on the rotational speed Ω and the misalignment \mathbf{a} , \mathbf{F}_p is the preload force coming from the external pressure support and \mathbf{F}_g is the gravity force. In addition, external forces \mathbf{F}_{ext} can act on the rotor. Note that the misalignment \mathbf{a} enters in the fluid equations by the kinematic relation ${}_B\mathbf{e} = \mathbf{r} - \mathbf{a}$ in Eq. (8).

As mentioned in Section 3, the preload force is assumed to be constant. For that reason and when no further forces are acting, the force \mathbf{F}_p has to compensate the gravity force all the time, in order to fulfill the definition of the misalignment \mathbf{a} at zero rotational speed; it gives $\mathbf{F}_p = -\mathbf{F}_g$.

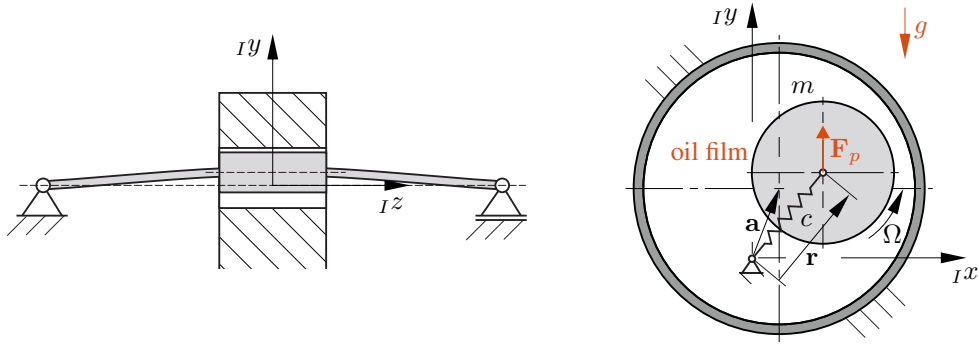


Figure 5: LAVAL rotor with misalignment, preload force and fluid forces.

For the model validation, the static equilibrium points at given rotational speeds Ω are considered. For the static deflection \bar{r} , following nonlinear equation has to be solved:

$$c\bar{r} = 2\mathbf{F}_f(\bar{r}, \Omega, \mathbf{a}). \quad (15)$$

Model A2: LAVAL Rotor with Misalignment and linearized Fluid Forces

For this rotor model, the LAVAL rotor is still used and the fluid forces are linearized around the equilibrium position \bar{r} , which is determined by the solution of Eq. (15) for a given rotational speed and a known misalignment, leading to:

$$\mathbf{F}_f(\mathbf{r}, \dot{\mathbf{r}}, \Omega, \mathbf{a}) \approx \mathbf{F}_f(\bar{r}, \Omega, \mathbf{a}) - \mathbf{K}_f(\bar{r}, \Omega, \mathbf{a})(\mathbf{r} - \bar{r}) - \mathbf{D}_f(\bar{r}, \Omega, \mathbf{a})\dot{\mathbf{r}}, \quad (16)$$

with the linearized matrices \mathbf{K}_f and \mathbf{D}_f for the fluid stiffness and damping, respectively. They are assumed to have the following form:

$$\mathbf{K}_f = -\frac{\partial \mathbf{F}_f}{\partial \mathbf{r}} \Big|_{\mathbf{r}=\bar{r}} = \begin{bmatrix} K_{xx} & k_{xy} \\ k_{yx} & K_{yy} \end{bmatrix}, \quad \mathbf{D}_f = -\frac{\partial \mathbf{F}_f}{\partial \dot{\mathbf{r}}} \Big|_{\mathbf{r}=\bar{r}} = \begin{bmatrix} D_{xx} & d_{xy} \\ d_{yx} & D_{yy} \end{bmatrix}, \quad (17)$$

where K is the direct stiffness, k the coupling stiffness, D the direct damping and d the coupling damping coefficient. Inserting Eq. (16) in Eq. (14) and using Eq. (15) gives the dynamic equations of the LAVAL rotor with misalignment and linearized fluid forces:

$$m\ddot{\mathbf{r}} + c(\mathbf{r} - \bar{\mathbf{r}}) + 2\mathbf{K}_f(\bar{\mathbf{r}}, \Omega, \mathbf{a})(\mathbf{r} - \bar{\mathbf{r}}) + 2\mathbf{D}_f(\bar{\mathbf{r}}, \Omega, \mathbf{a})\dot{\mathbf{r}} = \mathbf{F}_{ext}. \quad (18)$$

Model B1: Elastic Rotor with Misalignment and Fluid Forces

In a more detailed simulation model, the elastic deformation of the rotor is described by a set of mode shapes (Ritz ansatz). These mode shapes come from a finite element discretization of the rotor by using Bernoulli beam elements. For a better distinction from the LAVAL rotor, the elastic deformation is now described by the vector \mathbf{q} representing the modal coordinates. The dynamic behavior of the rotor is then characterized by the mass matrix \mathbf{M} and the stiffness matrix \mathbf{C} , leading for the rotor bearing system to:

$$\mathbf{M}\ddot{\mathbf{q}} + \mathbf{C}(\mathbf{q} - \bar{\mathbf{q}}) = \mathbf{F}_{f,1}(\mathbf{q}, \dot{\mathbf{q}}, \Omega, \mathbf{a}) + \mathbf{F}_{f,2}(\mathbf{q}, \dot{\mathbf{q}}, \Omega, \mathbf{a}) + \mathbf{F}_{ext}, \quad (19)$$

with the fluid forces $\mathbf{F}_{f,1}$ and $\mathbf{F}_{f,2}$ of the two bearings, external forces \mathbf{F}_{ext} and similar to the rotor models A1 and A2, a equilibrium position $\bar{\mathbf{q}}$. Damping or gyroscopic effects of the rotor are not considered.

Model B2: Elastic Rotor with Misalignment and linearized Fluid Forces

Similar to model A2, the fluid forces are linearized like in Eq. (16). Considering this in Eq. (19), following linear differential equation for the elastic rotor is obtained:

$$\mathbf{M}\ddot{\mathbf{q}} + \mathbf{C}(\mathbf{q} - \bar{\mathbf{q}}) + [\mathbf{K}_{f,1} + \mathbf{K}_{f,2}](\mathbf{q} - \bar{\mathbf{q}}) + [\mathbf{D}_{f,1} + \mathbf{D}_{f,2}]\dot{\mathbf{q}} = \mathbf{F}_{ext}, \quad (20)$$

which describes the motion of the rotor around the equilibrium position $\bar{\mathbf{q}}$.

5 Experimental Validation

In this section, an experimental validation of the rotor system of Section 3 is given by applying adequate simulation models of Section 4 depending on the specific accuracy requirements. A first experiment (static rotor equilibrium positions) is performed in order to determine the parallel misalignment between rotor and bearing axis. After having analyzed the misalignment, measurement data of a second experiment (rotor orbit at unbalance) is validated by simulation results of the four different simulation models of Section 4.

Experiment 1: Static Rotor Equilibrium Positions

The first experiment serves to determine the misalignment \mathbf{a} between rotor and bearing axis, which can not be identified by an absolute measurement.

On the test rig, the relative equilibrium positions of the rotor in the bearing can be measured for different rotational speeds Ω . Since the absolute position of the rotor can not be measured, the equilibrium positions are measured with respect to a reference position. The latter is chosen as the equilibrium position at high rotational speed, since it is known from theory that the rotor will be centered in the bearing housing for high rotational speeds [3].

The LAVAL-rotor model A1 with Eq. (15) for the equilibrium position $\bar{\mathbf{r}}$ is used for the experimental validation. With this model, an optimal misalignment parameter \mathbf{a} can be determined in such a way that the relative curve of equilibrium positions of the experiment is well approximated by the equilibrium positions calculated by Eq. (15).

In Fig. 6, the curve of equilibrium positions of the experiment and of the simulation can be seen. The misalignment parameter is chosen as $\mathbf{a} = [-0.15 \text{ mm}, 0.07 \text{ mm}]$. The measurement and the simulation start at $\Omega_1 = 3 \text{ rps}$ and move with increasing rotational speed to the reference position identical with the bearing center at $\Omega_2 = 100 \text{ rps}$.

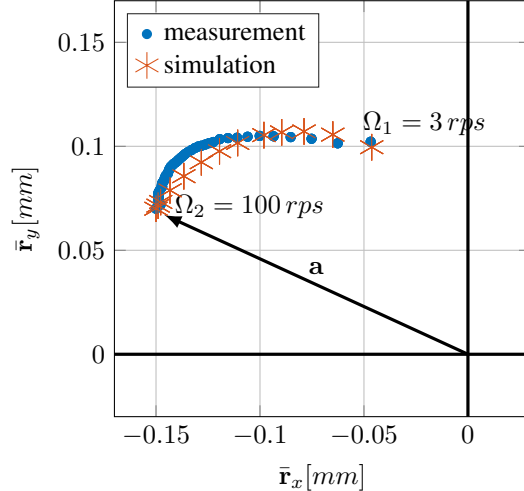


Figure 6: Measured and simulated curve of equilibrium positions with misalignment parameter $\mathbf{a} = [-0.15 \text{ mm}, 0.07 \text{ mm}]$.

When the equilibrium positions $\bar{\mathbf{r}}$ for different rotational speeds are known, the stiffness and damping coefficients of (17) can be calculated in a next step. Here, they are computed by a finite difference scheme and following mean coefficient can be determined:

$$K = (K_{xx} + K_{yy})/2, \quad k = (k_{xy} + k_{yx})/2, \quad D = (D_{xx} + D_{yy})/2, \quad d = (d_{xy} + d_{yx})/2.$$

The calculated as well as the measured mean coefficients are shown in Fig. 7. In the experiment, the coefficients are determined by exciting the rotor at different frequencies and measuring the rotor displacements and bearing reaction forces in the frequency domain. A fitting of the measured data by a reduced rotor bearing model gives the mean coefficient. The detailed measurement concept is described in [14]. Note that as far, only the mean values can be determined by this measuring method and hence, can be analyzed. The dependency of the measured coefficients on the rotational speed shows good agreement with the simulation results for the direct stiffness, direct damping and coupling stiffness coefficients (K , D and k). However, for the coupling damping coefficient d , a discrepancy is observed. The reason could be an angular misalignment of the rotor shaft in the experiment.

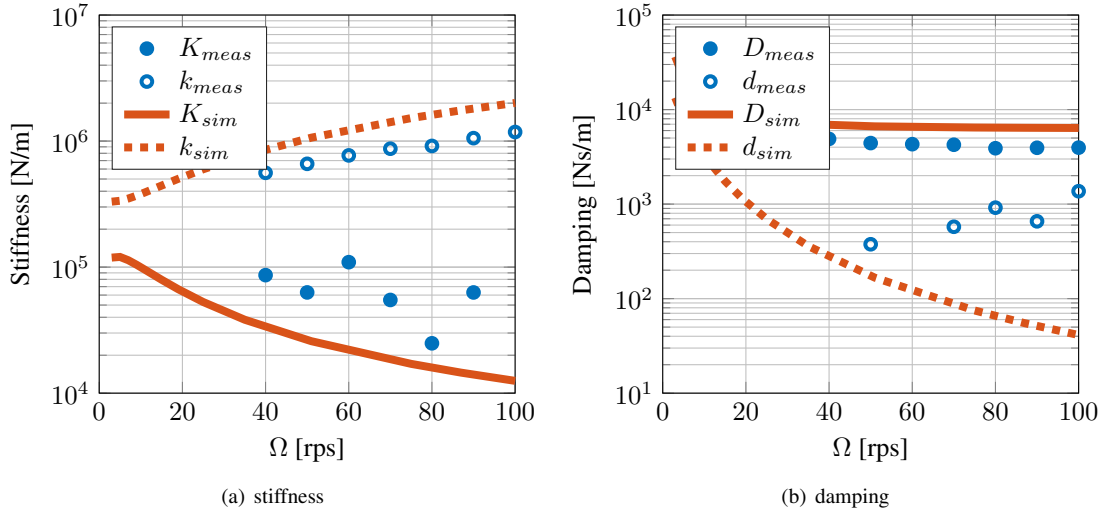


Figure 7: Calculated and measured stiffness and damping coefficients for different rotational speeds.

Experiment 2: Rotor Orbit at Unbalance

After having determined the parallel misalignment, a second experiment is performed in order to discuss the accuracy and efficiency of the four presented simulation models. Therefore, an unbalance is added at the middle of the rotor and the orbit of the rotor is measured at a constant rotational speed $\Omega = 21$ rps. The measured and simulated orbits are depicted in Fig. 8.

In Fig. 8(a), the measured and the simulated orbits are shown at their equilibrium positions. It has to be mentioned that the misalignment a determined by the first experiment is added to the measured orbit in order to get the absolute position of the orbit. The reason for that is that, as already mentioned, the absolute reference point of the measurement is unknown. For the simulation, rotor model A1 is used.

In Fig. 8(b), the form of the measured orbit is compared with the orbits obtained by the four simulation models. It can be seen that all four simulation models give nearly the same rotor orbit, meaning the model accuracy is sufficient for all simulation models. The elliptical form of the simulated orbits are characteristic for a rotor, which has an eccentric equilibrium position in the journal bearing. However, the form of the measured orbit has a tendency to a quadratic form. The reason could be that next to the unbalance an excitation with the third harmonic is present, which could cause a quadratic form, see for instance [13]. A physical source for a third harmonic excitation is usually caused by the three-jaw chuck during manufacturing of the rotor shaft.

When looking at the simulation time of the models in Table 2, it can be seen that the fastest model is model A2 – the LAVAL rotor model with linearized fluid forces. It is followed by the elastic rotor model B2, where the fluid forces are also linearized. A relatively long simulation time is needed for the full elastic rotor model B1 with nonlinear fluid forces. All the four simulation models are integrated with the `ode15s` solver of MATLAB, which uses a variable step size. The absolute and relative tolerance are set to $1e - 6$. For the elastic description of the rotor shafts of models B1 and B2, twelve RITZ modes are used.

Table 2: Simulation time for the different rotor models.

model	sim. time	rel. time
A1	11.7 s	100 %
A2	0.124 s	1.06 %
B1	1343 s	11478 %
B2	4.46 s	38.1 %

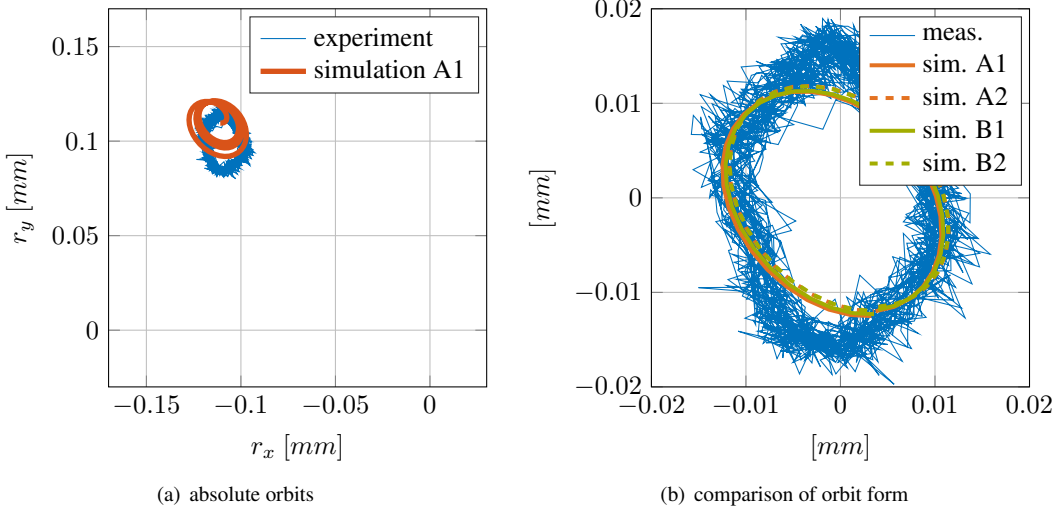


Figure 8: Rotor orbits due to unbalance at $\Omega = 21 \text{ rps}$.

6 Conclusion

In this contribution, a rotor test rig with two journal bearings is validated by adequate simulation models. It becomes evident that the misalignment of rotor and bearing axis has to be considered in the simulation models.

When using simulation models with nonlinear fluid forces (models A1 and B1), the misalignment has to be known for the dynamic simulation in order to ensure that the rotor moves in the simulation to the right equilibrium position. When using simulation models with linearized fluid forces (models A2 and B2), an important step for the dynamic analysis is the determination of the equilibrium position, which again requires the misalignment parameter. When the equilibrium position is known, the fluid forces can be linearized around this equilibrium position.

With respect to the accuracy of the simulation models, the LAVAL rotor model is accurate enough for the experimental validation presented in this contribution. The use of an elastic rotor is not necessary for the here described experiments, it only requires a larger modeling effort than the simple LAVAL rotor model.

The simulation costs can be saved significantly when the fluid forces are linearized, as the evaluation of the finite element solution of the nonlinear fluid forces are the most time-consuming part. However, the linearization has to be performed in a preprocessing step, as well as the calculation of the equilibrium position.

Outlook

For the model of the fluid forces, the classical REYNOLDS equation is applied, where effects of the fluid inertia are neglected. This assumption has to be analyzed further and comparisons with the bulk flow equations, usually applied for seals, should be made. Further, the effect of the preload force has to be investigated in more detail.

In this contribution, only mean stiffness and damping coefficients are determined in the experiment. Their practical relevance is only given for a vanishing eccentricity of the shaft. Usually, the exact coefficients have to be determined for a precise dynamic analysis, see the work of GLIENICKE [4] or SOMEYA [11].

The model based determination of the parallel misalignment as described in the first experiment could be further used for rotor diagnostics, similar to concepts described in [13].

References

- [1] Boedo, S. and Booker, J. (2004): Classical Bearing Misalignment and Edge Loading: A Numerical Study of Limiting Cases. *Tribology International*, **126**(3), pp. 535–541.

- [2] Chasalevris, A. and Dohnal, F. (2013): An Experimental Study on the Additional Harmonics due to Worn Journal Bearings. In *Tagungsband SIRM*, Magdeburg, Germany, Feb. 23-25.
- [3] Gasch, R., Nordmann, R. and Pfützner, H. (2006): *Rotordynamik*. Springer-Verlag, Berlin.
- [4] Glienicke, J. (1966): *Feder- und Dämpfungskonstanten von Gleitlagern für Turbomaschinen und deren Einfluß auf das Schwingungsverhalten eines einfachen Rotors*. PHD thesis, TH Karlsruhe.
- [5] Goenka, P.-K. (1984): Dynamically loaded journal bearings: finite element method analysis. *Journal of Tribology*, **106**(4), pp. 429–437.
- [6] Hamrock, B., Schmid, S. and Jacobson, B. (2004): *Fundamentals of fluid film lubrication*. CRC press, New York.
- [7] Hu, W., Miah, H., Feng, N. and Hahn, E. (2000): A rig for testing lateral misalignment effects in a flexible rotor supported on three or more hydrodynamic journal bearings. *Tribology International*, **33**(3), pp. 197–204.
- [8] Krinner, A., Schindler, T. and Rixen D. J. (2016): Time integration of mechanical system with elastohydrodynamic joints using Quasi-Newton method and projection formulation. *International Journal of Numerical Methods in Engineering*.
- [9] Nikolakopoulos, P. and Papadopoulos C. (2008): A study of friction in worn misaligned journal bearings under severe hydrodynamic lubrication. *Tribology International*, **41**(6), pp. 461–472.
- [10] Pennacchi, P., Vania, A. and Chatterton, S. (2011): Analysis of the Effects of Parallel and Angular Misalignment in Hyperstatic Rotors Equipped With Oil-Film Bearings. In *Proceedings of the ASME Turbo Expo*. Vancouver, British Columbia, Canada, June 6–10.
- [11] Someya, T. (1989): *Journal-Bearing Databook*. Springer-Verlag, Berlin, Heidelberg.
- [12] Sun, J. and Changlin, P. (2004): Hydrodynamic lubrication analysis of journal bearing considering misalignment caused by shaft deformation. *Tribology International*, **37**(10), pp. 841–848.
- [13] Thümmel, T., Roßner, M., Ulbrich, H. and Rixen, D. (2015): Unterscheidung verschiedener Fehlerarten beim modellbasierten Monitoring. In *Tagungsband SIRM*, Magdeburg, Germany, Feb. 23-25.
- [14] Wagner, C., Tsunoda, W., Berninger, T., Thümmel, T. and Rixen, D. (2017): Instability Prediction and Rotordynamic with Seals: Simulations Based on the Bulk-Flow Theory and Experimental Measurements. In *Proc. of DINAME 2017*. Sao Sebastiao, Sao Paulo, Brasil, March 5–10.

Address: Chair of Applied Mechanics, Technical University of Munich, 85748 Garching, Germany,
 email: andreas.krinner@tum.de